Journal of Catalysis 285 (2012) 61–73

Contents lists available at SciVerse ScienceDirect

Journal of Catalysis

journal homepage: www.elsevier.com/locate/jcat

On the structure dependence of CO oxidation over CeO_2 nanocrystals with well-defined surface planes

Zili Wu [a,b,*], Meijun Li [a], Steven H. Overbury [a,b,*]

[a] Chemical Science Division, Oak Ridge National Laboratory, Oak Ridge, TN 37831, United States
[b] Center for Nanophase Materials Sciences, Oak Ridge National Laboratory, Oak Ridge, TN 37831, United States

ARTICLE INFO

Article history:
Received 12 July 2011
Revised 6 September 2011
Accepted 12 September 2011
Available online 14 October 2011

Keywords:
Ceria nanoshapes
Rods
Cubes
Octahedra
CO oxidation
Structure dependence
In situ spectroscopy
Reaction mechanism

ABSTRACT

CO oxidation is a model reaction for probing the redox property of ceria-based catalysts. In this study, CO oxidation was investigated over ceria nanocrystals with defined surface planes (nanoshapes) including rods ({1 1 0} + {1 0 0}), cubes ({1 0 0}), and octahedra ({1 1 1}). To understand the strong dependence of CO oxidation observed on these different ceria nanoshapes, *in situ* techniques including infrared and Raman spectroscopy coupled with online mass spectrometer, and temperature-programmed reduction (TPR) were employed to reveal how CO interacts with the different ceria surfaces, while the mobility of ceria lattice oxygen was investigated *via* oxygen isotopic exchange experiment. CO adsorption at room temperature leads to strongly bonded carbonate species on the more reactive surfaces of rods and cubes but weakly bonded ones on the rather inert octahedra surface. CO-TPR, proceeding *via* several channels including CO removal of lattice oxygen, surface water–gas shift reaction, and CO disproportionation reaction, reveals that the reducibility of these ceria nanoshapes is in line with their CO oxidation activity, i.e., rods > cubes > octahedra. The mobility of lattice oxygen also shows similar dependence. It is suggested that surface oxygen vacancy formation energy, defect sites, and coordinatively unsaturated sites on ceria play a direct role in facilitating both CO interaction with ceria surface and the reactivity and mobility of lattice oxygen. The oxygen vacancy formation energy, nature and amount of the defect and low coordination sites are intrinsically affected by the surface planes of the ceria nanoshapes. Several reaction pathways for CO oxidation over the ceria nanoshapes are proposed, and certain types of carbonates, especially those associated with reduced ceria surface, are considered among the reaction intermediates to form CO_2, while the majority of carbonate species observed under CO oxidation condition are believed to be spectators.

1. Introduction

Cerium oxide and ceria-containing materials have received intense investigation as catalysts and catalyst supports for use in variety of catalytic reactions [1–9]. These applications generally take advantage of the excellent redox property and high oxygen storage capacity (OSC) of ceria. Therefore, great effort has been devoted to understanding the special redox property of ceria and to exploring ways to improve this property [10–18]. CO oxidation, a primary function of three-way catalytic convertors containing ceria catalysts, is a prototype model reaction for probing the redox property of ceria catalysts. CO oxidation is believed to proceed *via* Mars–van Krevelen mechanism over ceria [1,19], namely, it involves the removal of surface lattice oxygen by CO and consequent annihilation of vacancies by gas phase oxygen. The removal of surface oxygen, i.e., oxygen vacancy formation, is the rate determination step (RDS) since the reoxidation with O_2 is very facile for reduced ceria. Extensive experimental and theoretical studies have been devoted to understanding CO oxidation over ceria catalysts [11,15,17,20–28]. A general consensus has been reached that CO interaction with ceria is structure dependent. Previous studies on polycrystalline ceria with differently exposed crystal planes already implied that CO oxidation is structure sensitive on ceria [17]. Recently, thanks to the advance of nanomaterial synthesis, ceria nanocrystals with controlled crystallographic planes [11,15,16,28–32] such as ceria rods and cubes, exposing crystal planes of {1 1 0} + {1 0 0} and {1 0 0}, respectively, have been successfully obtained and compared with multifaceted ceria nanoparticles for CO oxidation. It has been shown that ceria nanocrystals exposing reactive {1 1 0} and {1 0 0} planes on the surface are more active for CO oxidation than those dominated by {1 1 1} surfaces. The structure dependence of CO oxidation activity is explained largely based on theoretical work [33,34], which suggests that the oxygen vacancy formation energy is surface sensitive, following the sequence {1 1 0} < {1 0 0} < {1 1 1}. In order to understand the CO oxidation mechanism over different ceria surfaces, a number of theoretical studies have been dedicated to the

---

* Corresponding authors. Address: Chemical Science Division, Oak Ridge National Laboratory, Oak Ridge, TN 37831, United States.
E-mail addresses: wuz1@ornl.gov (Z. Wu), overburysh@ornl.gov (S.H. Overbury).

0021-9517/$ - see front matter © 2011 Elsevier Inc. All rights reserved.
doi:10.1016/j.jcat.2011.09.011

interaction between CO and ceria surfaces [22,23,25–27,35–37]. The calculations show structure selectivity for CO adsorption, predicting weak CO adsorption for the most stable {1 1 1} surface and stronger chemisorption on more open surfaces, such as the {1 1 0} and {1 0 0}. The strong binding of CO to these ceria surfaces is mediated by the formation of carbonate-like complexes [23]. These investigations point to the direction of improving the redox property of ceria catalysts *via* utilizing ceria nanocrystals with more open surface structures.

Despite the intensive experimental and theoretical studies of CO adsorption and oxidation on ceria catalysts, there is still a lack of spectroscopic investigation of how CO interacts with different ceria surfaces and what the reaction mechanism is. Also lacking is the understanding of how the surface and bulk oxygen reactivity and mobility are affected by the surface structure of ceria, which could also have an impact on CO oxidation behavior. In this work, along the lines of our recent work [10] using ceria nanocrystals with define surface structures (nanoshapes), *in situ* vibrational spectroscopy including infrared and Raman will be employed to study the nature of the interaction of CO with three distinct ceria nanoshapes: rods ({1 1 0} + {1 0 0}), cubes ({1 0 0}), octahedra ({1 1 1}). We provide molecular-level insights into the surface dependence of CO oxidation over ceria catalyst and the mechanism of CO oxidation. Our results show that CO adsorption and reaction with ceria, and the reactivity and mobility of lattice oxygen are strongly influenced by the surface structure of ceria, thus leading to the nanoshape dependence of CO oxidation. The majority of carbonate species observed under steady state CO oxidation are reaction spectators while carbonate species associated with reduced Ce cations are possibly among the reaction intermediates in CO oxidation over ceria catalysts.

2. Experimental

2.1. Material synthesis

The synthesis of the three ceria nanoshapes has been described in detail in our recent paper [10]. Briefly, CeO_2 octahedra, rods, and cubes were prepared by hydrothermal process [16,29] in Teflon-lined stainless steel autoclaves at different hydrothermal temperatures and durations. For CeO_2 octahedra, 0.434 g $Ce(NO_3)_3 \cdot 6H_2O$ (ARCOS, 99.50%) and 0.0038 g $Na_3PO_4 \cdot 12H_2O$ (EM Science) precursors were used. 0.868 g of $Ce(NO_3)_3 \cdot 6H_2O$ and 9.6 g NaOH (BDH) were used as precursors to obtain ceria rods and cubes. After the hydrothermal treatment, fresh white precipitates were separated by centrifugation, washed with deionized water and ethanol several times, followed by drying at 333 K in air overnight. Nitrate species were detected on ceria rods and cubes while phosphate species on octahedra by Raman spectroscopy [10]. The amount of P on the ceria octahedra surface was determined by XPS to be small (P/Ce atomic ratio around 0.16). Although P has been found detrimental to the redox property of ceria catalyst, previous study indicated that the effect is relatively limited at XPS P/Ce ratio <0.2 (corresponding to bulk P/Ce < 0.03) [38]. So it is still reasonable to attribute our experimental observations largely to the surface structure effect of octahedra rather than P poisoning.

2.2. Material characterizations

XRD patterns of the ceria nanocrystals were collected on a PANalytical powder diffractometer using Cu Kα radiation. The electron microscopy images of the ceria nanocrystals were recorded on a Zeiss Libra 120 TEM and Zeiss Merlin VP SEM/STEM systems. Brunauer–Emmett–Teller (BET) surface area of the 623 K calcined ceria nanocrystals was measured *via* nitrogen adsorption at 77 K by using a Micromeritic Gemini 275 system.

2.3. CO oxidation performance

CO oxidation over the ceria nanoshapes was tested on a plug-flow, temperature-controlled microreactor system (Altamira AMI 200). The sample (ca. 50 mg) was well-mixed and diluted with quartz sand to a similar volume to minimize diffusion limitations. The sample, loaded into a U-shaped quartz tube (4 mm i.d.) and supported by quartz wool, was pretreated in flowing 5% O_2/He (30 mL/min) at 673 K for 1 h and cooled down to room temperature (rt) in O_2/He atmosphere. The gas was switched to the reaction mixture (30 mL/min 5% O_2/He + 10 mL/min 2% CO/2%Ar/He; O_2: CO = 7.5) at rt, and the system was ramped up to 673 K and cooled back to rt at a rate of 1 K/min. A portion of the product gas stream was extracted periodically with an automatic sampling valve and analyzed using a dual-column gas chromatograph with a thermal conductivity detector. All gases, unless specified, were provided by Air Liquide with the UHP helium as balance gas, with moisture content less than 1 ppm.

2.4. Temperature-programmed reduction and desorption (TPR and TPD) and oxygen isotopic exchange

CO-TPR, TPD, and oxygen isotopic exchange over ceria samples (ca. 30 mg) were also conducted on the AMI microreactor system. Before each of the experiments, the ceria sample was pretreated in flowing 5% O_2/He (30 mL/min) at 673 K for 1 h and cooled down to rt and switched to helium purging for 30 min.

- For TPD, the pretreated sample was exposed to 2% CO/2%Ar/He (30 mL/min) at rt for 30 min and then purged with helium at rt for 45 min. Then the sample was heated (10 K/min) up to 690 K in flowing helium and hold for another 30 min.
- For CO-TPR, the pretreated sample was exposed to 2% CO/2%Ar/He (30 mL/min) at rt for 30 min and then ramped (10 K/min) up to 1073 K and held for another 30 min. In both CO-TPR and CO-TPD, the gas stream was analyzed by an online quadrupole mass spectrometer (QMS) (OmniStar GSD-301 O2, Pfeiffer Vacuum).
- For oxygen isotopic exchange, the pretreated sample was exposed to 1% $^{18}O_2$/He (30 mL/min) at rt and ramped (10 K/min) up to 1100 K. The oxygen isotopomers (32, 34, and 36) were monitored by the online QMS.

2.5. In situ spectroscopy

IR spectra were collected using a Thermo Nicolet Nexus 670 spectrometer in diffuse reflectance mode (DRIFTS) while the exiting stream was analyzed by QMS [39,40]. A Pike Technologies HC-900 DRIFTS cell with nominal cell volume of 6 cm^3 was used. Before each of the following IR experiments, the ceria sample was pretreated in the DRIFTS cell in flowing 2% O_2/He (25 mL/min) at 693 K for 1 h and then cooled to rt before switching to He.

- In CO adsorption experiments, the pretreated sample was purged with helium at rt before switching to 2%CO/2%Ar/He (25 mL/min) flow for 30 min.
- In temperature-programmed reduction experiments (CO-TPR-IR), the pretreated ceria sample was exposed to flowing 2%CO/2%Ar/He (25 mL/min) for 30 min at rt and then ramped (10 K/min) up to 773 K in the same gas.
- In CO oxidation experiments, the ceria sample was pretreated at 693 K, purged in He at 693 K and then exposed to the reaction mixture (20 mL/min 2% O_2/He and 5 mL/min 2%CO/2%Ar/He;

O_2:CO = 4). The O_2/He and CO/Ar/He flows were switched off and on separately to allow monitoring surface species change. Switching between 2% $^{18}O_2$/He (Isotech, $^{18}O_2$ purity of 99%) and 2% $^{16}O_2$/He was also done during CO oxidation reaction.

IR spectra and QMS profiles were recorded continuously during these processes. All reported IR spectra are difference spectra referenced to a background spectrum collected after pretreatment but prior to CO adsorption/oxidation. For CO-TPR-IR, the IR spectra were referenced to the background spectra collected at the same temperature during cooling down from pretreatment process.

The CO-TPR process on ceria samples was also monitored by *in situ* Raman spectroscopy (CO-TPR-Raman). The ceria sample was pretreated in a Raman catalytic reactor (Linkam CCR1000) in flowing 2% O_2/He (30 mL/min) at 673 K for 1 h and cooled down to rt and purged with He (30 mL/min). The sample was then exposed to 1%CO/He (30 mL/min) flow for 30 min at rt and then ramped (10 K/min) up to 773 K in the same atmosphere for CO-TPR-Raman study. Raman scattering was collected *via* a customized ellipsoidal mirror and directed by a fiber optics bundle (Princeton Instruments) to the spectrograph stage of a triple Raman spectrometer (Princeton Instruments Acton Trivista 555) [41]. Edge filters (Semrock) were used in front of the UV–vis fiber optic bundle to block the laser irradiation. The 532-nm excitation (20 mW at sample) was emitted from a solid state laser (Princeton Scientific, MSL 532-50). A UV-enhanced liquid N_2-cooled CCD detector (Princeton Instrument) was employed for signal detection. The Raman reactor sits on an XY stage (Prior Scientific, OptiScan XY system) and translates in raster mode while collecting the spectrum. The fast translation has shown been able to eliminate/minimize any laser damage of the samples. Cyclohexane was used as a standard for the calibration of the Raman shifts.

3. Results

3.1. Structure of ceria nanocrystals studied by XRD, TEM, and BET

Measured XRD patterns and TEM images of the three ceria polymorphs were similar to those reported in our previous work [10] and are not shown here for brevity. Their XRD patterns can be indexed to the pure fluorite cubic structures (space group Fm3m (225), JCPDS 34-0394). The cubes and octahedra exhibit sharper XRD peaks than the rods, and the mean particle sizes, determined from the Scherrer equation, are 11, 43, and 72 nm for rods, cubes, and octahedra, respectively. The high-resolution electron micrographs of the nanoshapes before reaction [10] show that the cubes expose {1 0 0} surfaces and octahedra expose {1 1 1} surfaces, in agreement with their geometric shapes and previous studies of ceria nanomaterials [15,16,29]. Although previous work [10,15,16,29] has concluded that the rods consist of a mixture of {1 1 0} and {1 0 0} surfaces (ca. 50% of each), the micrographs [10] showed that the rods used in our study are also characterized as having higher concentration of dark area than the cubes and octahedra, likely due to the presence of concentrated coordinatively unsaturated (*cus*) sites. Fig. 1 shows electron micrographs of the ceria nanocrystals after exposure to CO oxidation reaction conditions at 673 K. No evident change of the morphology is observed for the three nanoshapes, consistent with our previous observation that the three ceria polymorphs are thermally stable at temperatures up to 773 K [10]. To keep the morphology and surface structure intact, measurements on the three ceria nanoshapes were carried out at temperatures lower than 773 K, except in some temperature-programmed experiments (such as CO-TPR) where samples were sacrificed by heating to higher temperatures. The BET areas of the rods, cubes, and octahedra are measured to be 93, 29, and 12 m^2/g, respectively.

3.2. Catalytic CO oxidation

Fig. 2A exhibits the light-off curves from CO oxidation over the three ceria nanoshapes based on equal reactor sample weight. Rods are the most active, followed by cubes with octahedra the least active. For example, the temperature for 20% CO conversion is 533 K on rods, 593 K on cubes, and 686 K on octahedra. Since the three nanoshapes have well-defined surface terminations and known surface area, it is possible to compare the CO oxidation activity on the basis of surface sites. Taking into account the different surface oxygen densities [10,42] and assuming the equal composition of {1 1 0} and {1 0 0} on rods surface [15,16], the CO turnover frequency on the basis of surface oxygen sites (TOF, converted CO per surface O per second) is compared in Fig. 2B for the three surfaces, {1 1 0}, {1 0 0}, and {1 1 1}. To maintain differential conditions, the CO TOF is calculated only in the low conversion regime (<15%). The structure dependence of CO oxidation over ceria nanocrystals is clearly demonstrated, i.e., {1 1 0} > {1 0 0} > {1 1 1}. There is no deactivation of the ceria nanoshapes during CO oxidation because the CO conversion curves during heating and subsequent cooling coincide (see Fig. S1 in supporting information).

To understand the surface structure dependence of CO oxidation over the ceria nanoshapes, it is necessary to study how the two reactants, CO and O_2, behave when interacting with different ceria surfaces. For CO, its adsorption on ceria and reduction of ceria was followed by *in situ* IR and Raman spectroscopy. For oxygen, it is the lattice oxygen rather than the adsorbed or gaseous oxygen that is relevant to CO oxidation under typical high reaction temperatures. So, the reactivity and mobility of lattice oxygen were studied by isotopic exchange.

3.3. Adsorption of CO studied by IR spectroscopy

Fig. 3A shows the IR spectra from CO adsorption on ceria rods at rt as a function of time after switching in the CO feed. In the region above 2000 cm^{-1}, the development of a rather sharp band at 2172 cm^{-1}, due to adsorbed CO on surface *cus* Ce^{4+} [2,43], is observed superimposed upon the gas phase CO bands as more CO is exposed to the sample. CO is weakly held on *cus* Ce^{4+} sites, and the 2172 cm^{-1} band disappears rapidly upon removing CO feed. No IR bands due to adsorbed or gas phase CO_2 are observed. CO interacts strongly with the surface oxygen and forms a variety of carbonate species as evident from the development of a series of IR bands in the range from 1800 to 800 cm^{-1}. This is similar to previous investigations of CO adsorption on polycrystalline ceria [2,43]. The assignments are made in Table 1 based on previous studies of CO and CO_2 adsorption on ceria [2,43–48]. Bicarbonate species (864, 1216, 1395, 1616, and 3619 cm^{-1}), bidentate carbonate species (864, 1024, 1265, and 1647 cm^{-1}), and bridged carbonate species (1024, 1265, and 1695 cm^{-1}) are formed upon CO interaction with the surface oxygen of ceria rods.

Fig. 3B compares the IR spectra of the three ceria nanoshapes after adsorption of CO at rt for 30 min (see Fig. S2 for CO adsorption on ceria cubes and octahedra as a function of time). No production of CO_2 is observed on any sample, and CO is only weakly adsorbed on surface *cus* Ce^{4+} cations. But the relative intensity of the band at 2172 cm^{-1} to the CO gas phase bands is clearly different on the three samples, indicating the amount of CO adsorbed on *cus* Ce^{4+} sites follows the trend: rods > cubes > octahedra. Carbonate species are formed on all three surfaces. Similar carbonate species are observed on both rods and cubes surfaces since the spectral features below 2000 cm^{-1} on the two samples are quite similar to each other, while different types of carbonate species occur on the octahedra surface. The specific assignments of the spectral features are listed in Table 1.

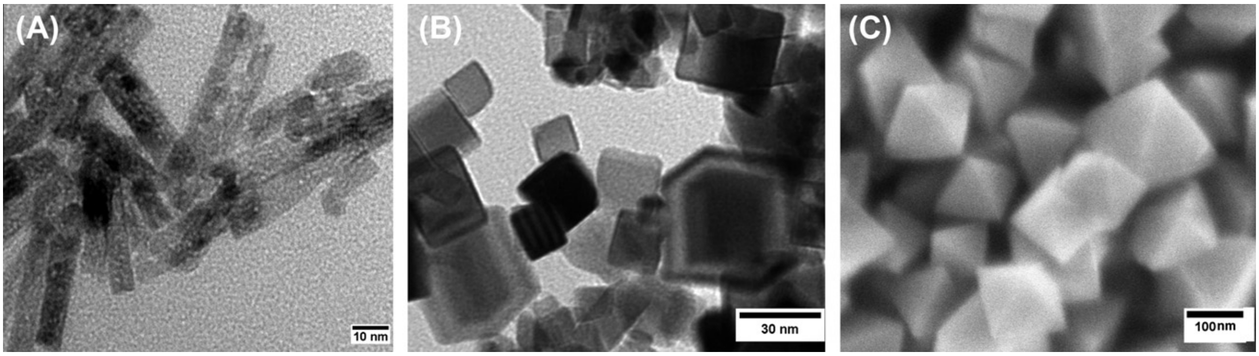

Fig. 1. TEM images of ceria rods (A, scale bar 10 nm), cubes (B, scale bar 30 nm) and SEM image of octahedra (C, scale bar 100 nm) after CO oxidation to 673 K.

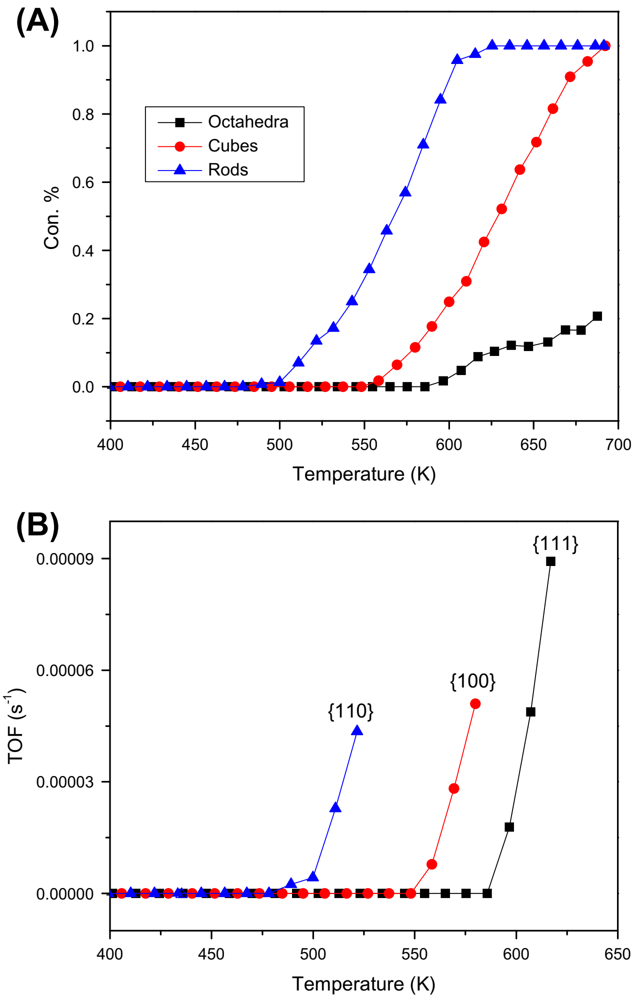

Fig. 2. (A) Light-off curves for CO oxidation over ceria rods, cubes, and octahedra. Based on same catalyst weight (~50 mg). Reaction feed: 10 mL/min 2%CO/Ar/He + 30 mL/min 5% O_2/He. (B) Comparison of CO TOF (converted CO per surface O per s) over three ceria surface planes, {1 1 0}, {1 0 0}, and {1 1 1}.

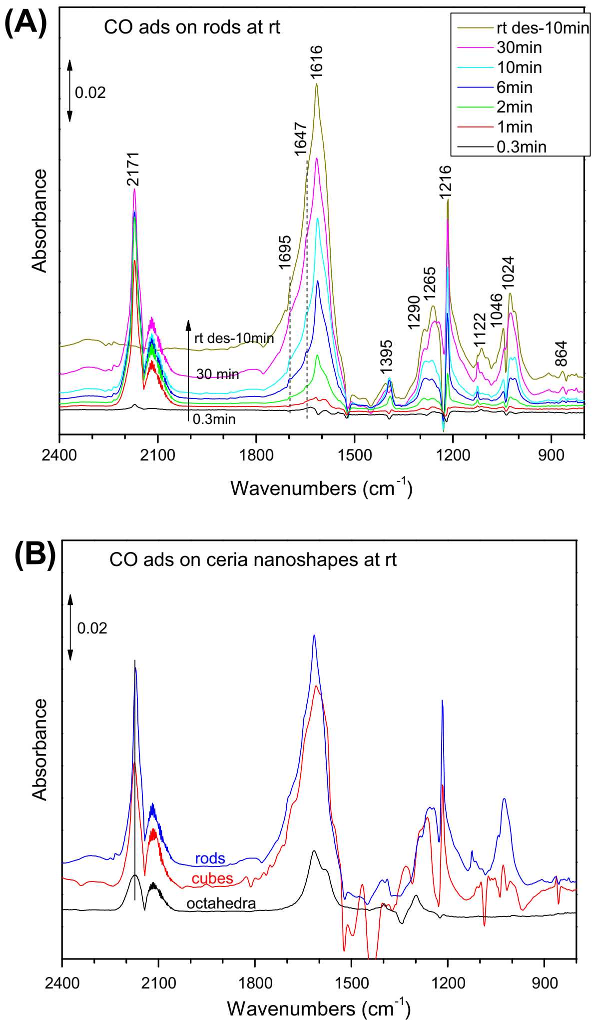

Fig. 3. (A) IR spectra of CO adsorbed on ceria rods at rt as a function of time after start of CO adsorption. (B) Comparison of CO adsorbed on three ceria nanoshapes at rt after 30 min adsorption. Spectra are referenced to a pretreated sample in He prior to introducing the CO flow. (For color interpretation in this figure the reader is referred to see the web version of this article.)

To investigate how strongly the carbonate species are held on the three ceria nanoshapes, temperature-programmed desorption (TPD) in helium was conducted after CO exposure at rt for 30 min on the ceria samples. The evolution of both CO and CO_2 was monitored by online QMS, but there was essentially no CO desorption observed from the three samples during TPD process. CO_2 is the major product, due to the thermal decomposition of surface carbonate species. Its appearance in TPD implies reduction of the ceria surfaces. As compared in Fig. 4, both rods and cubes show CO_2 desorption over a wide temperature range and the desorption still continues while holding at the final desorption temperature (690 K), indicating the existence of both weakly and strongly held carbonate species on these two surfaces. The roughly similar CO_2 desorption behavior is consistent with the IR observation of similar surface carbonate species on rods and cubes. Octahedra show a

Table 1
Assignment of IR bands observed upon room temperature CO adsorption on ceria nanoshapes.

Sample	Species	ν (CO_3)	π (CO_3)	δ (OH)	ν (OH)
Rods	Bicarbonate	1395, 1616	864	1216	3619
	Bidentate carbonate	1024, 1265, 1647	864		
	Bridged carbonate	1024, 1122, 1265, 1695			
Cubes	Bicarbonate	1056, 1392, 1611	862	1216	3619
	Bidentate carbonate	1030, 1281, 1572	862		
	Bridged carbonate	1030, 1124, 1281, 1688			
Octahedra	Bidentate carbonate	1298, 1616			
	Unidentate carbonate	1400, 1578			

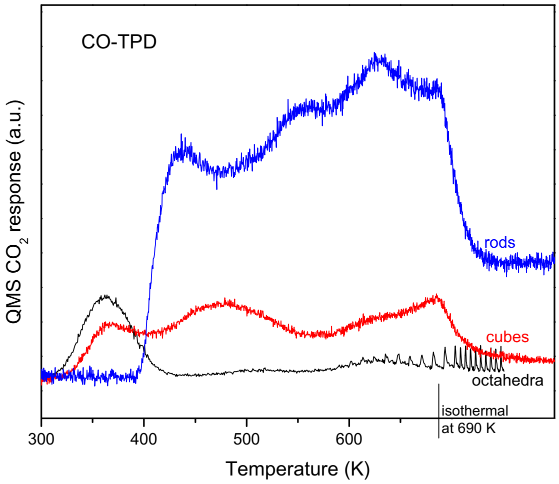

Fig. 4. CO_2 evolution during CO-TPD in helium on three ceria nanoshapes after CO adsorption at rt for 30 min. The sharp peaks at high temperature on the octahedra are an artifact of the QMS.

main CO_2 desorption peak at temperature below 400 K and a smaller desorption peak above 600 K. Apparently, weakly held carbonate is dominant on the octahedra surface. The TPD profiles suggest that the strong interaction between CO and the more open {1 1 0} and {1 0 0} surfaces leads to more thermally stable carbonate species on ceria rods and cubes.

3.4. CO-TPR studied by IR and Raman

Fig. 5A shows CO_2 profiles evolved during CO-TPR of the three ceria nanoshapes normalized on weight basis. All samples exhibit low- (<850 K) and high-temperature (>850 K) reduction regimes, due to the removal of surface oxygen and bulk oxygen as in the case of H_2-TPR [1], respectively. Of note, the low-temperature peak of CO_2 evolution closely matches the temperatures for the onset of CO oxidation (Fig. 2A) for each nanoshape and is thus of interest for CO oxidation reaction. The more intense and broader low-temperature CO_2 peaks at 570 and 740 K for rods indicate the presence of large amount of reactive oxygen on the surface of the rods. The cubes show a low-temperature CO_2 peak (570 K) with extension to higher temperatures, while octahedra only show a rather broad high-temperature peak at 740 K. Evolution of H_2 is also observed during CO-TPR of ceria samples and is presented in Fig. 5B. H_2 production is due to the reaction between surface OH groups and CO *via* water–gas shift type reactions [49,50]:

$$CO + OH \rightarrow 0.5H_2 + CO_2 \quad (1)$$

$$CO + 2OH \rightarrow H_2 + CO_2 + O_L \quad (2)$$

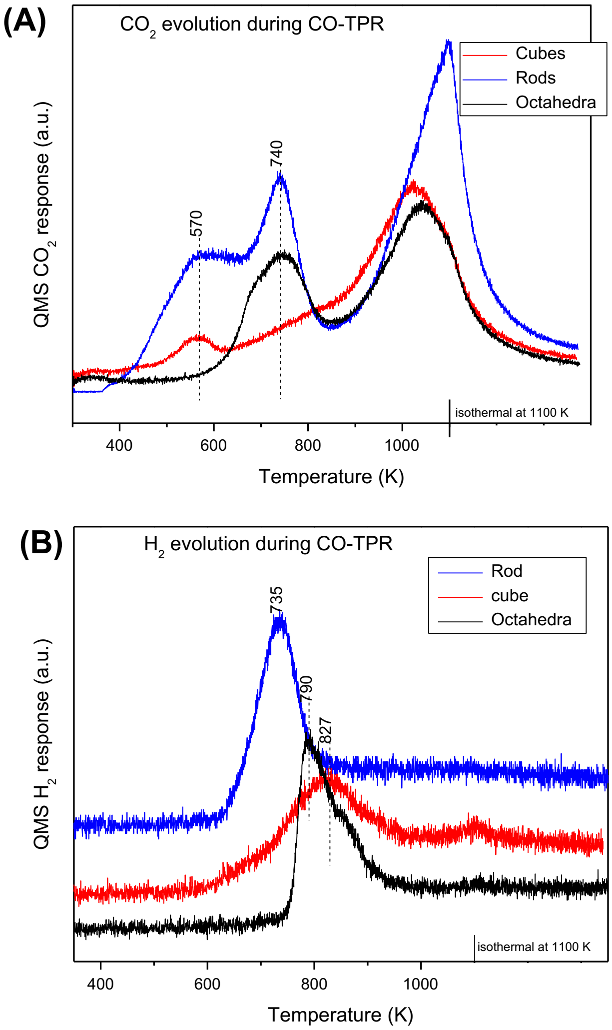

Fig. 5. CO_2 (A) and H_2 (B) evolution during CO-TPR over three ceria nanoshapes.

The temperature of H_2 evolution roughly coincides with the temperature of CO_2 production at the higher temperature range (650–850 K). The amount of CO_2 evolved from these surface reactions is determined to be more than 50% to the total CO_2 production in the low-temperature range (300–850 K) on the three ceria nanoshapes (see Table S1 for details). The CO_2 peak at 570 K in CO-TPR of rods and cubes seems to be due to CO reaction with reactive surface lattice oxygen (O_L),

$$CO + O_L \rightarrow CO_2 \quad (3)$$

while the higher temperature peak at ~740 K is the combination of CO reaction with both surface hydroxyl groups and lattice oxygen. The presence of one broad peak at 740 K for octahedra indicates that the surface lattice oxygen and surface OH groups are close in reactivity to CO on the {1 1 1} surface.

In situ DRIFTS and Raman spectroscopy were employed to monitor surface species evolved during CO-TPR of the ceria samples up to 773 K. IR spectra of rods during CO-TPR are shown in Fig. 6a–f. The rt spectrum is the same as shown in Fig. 3 for CO adsorption, exhibiting features due to adsorbed CO on surface *cus* Ce^{4+} sites and a variety of surface carbonate species (bicarbonate, bidentate, and bridged carbonate). Changes in the spectra are observed in the following three regions as the CO-TPR temperature rises. First, in the 3800 to 2600 cm^{-1} region, bands characteristic of formate (2965, 2932, 2842 cm^{-1}) and derived from reaction between CO and surface OH groups [44,45,48] start to appear at 373 K. The band at 2965 cm^{-1}, due to bridged formate [44], grows in intensity at low temperature and then gives way to the bands at 2932 and 2842 cm^{-1} due to bidentate formate [44] at higher temperatures. The bidentate formate reaches maximum amount at around 573 K and disappears at 773 K as evident from the IR bands intensity change. Formyl species, a proposed intermediate to formate [45,51], is also observed at 573 K with an IR band at 2721 cm^{-1}. Negative-going features above 3300 cm^{-1} are observed to accompany the evolution of IR bands of formate as a function of temperature, in accordance with the consumption of OH groups in the creation of formate species. Specifically, negative features include a broad band below 3600 cm^{-1} due to hydrogen-bonded OH groups, three sharp bands at 3623, 3642, and 3711 cm^{-1} due to type III, II, and I hydroxyl groups [2], respectively. Second, in the region from 2500 to 2000 cm^{-1}, the peak due to weakly held CO on surface *cus* Ce^{4+} sites (2172 cm^{-1}) disappears below 373 K. This spectral region is dominated by gas phase CO bands at temperature above 373 K. A broad and elevated background extending from 2000 to 3000 cm^{-1} appears at 673 K. This broad feature is most prominent at 773 K and is due to electronic absorption in reduced ceria, a characteristic semiconductive property observed on ceria [2] and other semiconductors such as ZnO and TiO_2 [52,53]. Its appearance is an indication of the reduction of ceria (Ce^{4+} to Ce^{3+}) by CO. Third, in the region from 2000 to 800 cm^{-1}, the spectra show subtle changes in intensity as a function of temperature. This is due to the fact that carbonates decomposition and new carbonates formation (*via* CO interaction with surface oxygen) are taking place simultaneously and both events are promoted by elevated temperatures. The sharp peak at 1216 cm^{-1}, characteristic of bicarbonate, disappears above 473 K. The IR features observed at 773 K can be assigned roughly to a mixture of unidentate (1600, 1404, 1078, 863 cm^{-1}), bidentate (1600, 1267, 1048, 863 cm^{-1}), and bridged (1781, 1404, 1195 cm^{-1}) carbonate species.

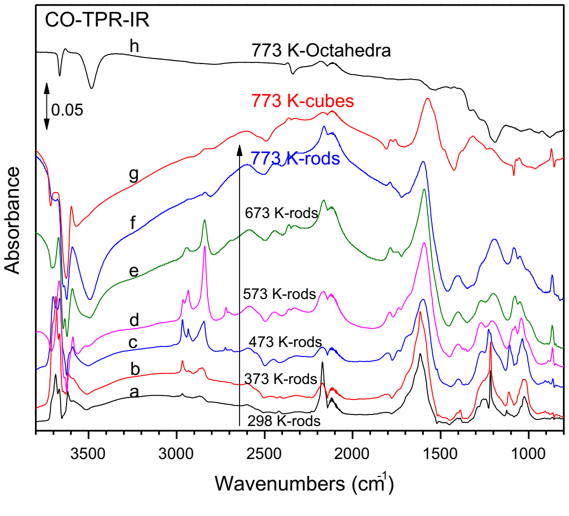

Fig. 6. IR spectra collected during CO-TPR of ceria rods at different temperature (a–f) and cubes (g) and octahedra (h) at 773 K. Spectra are referenced to the background spectra collected at the indicated temperature during cooling down from pretreatment process of the ceria sample.

Similar spectral changes, but with different degree of changes, are also observed in the CO-TPR-IR spectra of ceria cubes and octahedra (see Fig. S3). For comparison, CO-TPR-IR 773 K spectra for cubes and octahedra are shown in Fig. 6g and h. The 773 K spectra of rods and cubes are similar to each other, featuring a broad background due to the reduction of ceria, and evolution of a mixture of carbonate species. However, two clear differences can be seen between these two and octahedra. First, there is hardly an elevated spectral background for octahedra, suggesting less reduction of octahedra by CO. Second, IR bands due to carbonate species are barely observable on octahedra. This is consistent with the CO-TPD observation that carbonate species are weakly held on octahedra surface and unstable at 773 K.

Fig. 7A exhibits the Raman spectra collected during CO-TPR to 773 K on ceria rods in the spectral range below 2000 cm^{-1}. Before exposing to CO, ceria shows a characteristic strong band at 462 cm^{-1} with weak bands near 590 and 1180 cm^{-1}, due to lattice oxygen motion (F_{2g} mode), defect sites, and second-order longitudinal optical (2LO) mode, respectively [10,54]. During CO-TPR, two broad bands centered at 1350 and 1600 cm^{-1} start to form at temperature of 673 K and grow in intensity as a function of reduction time and temperature. They dominate the Raman spectra at 773 K and are even stronger than the attenuated ceria F_{2g} band (462 cm^{-1}). According to their frequency, they could be due either to surface carbonate or to a carbonaceous species. However, two experimental observations support their assignment to carbonaceous species. First, the Raman spectra of ceria rods were affected differently when exposed to either He or O_2 purging at 673 K after CO-TPR. As compared in Fig. 7B, the spectra are essentially the same before and after He purging, but the two bands at 1350 and 1600 cm^{-1} are completely eliminated after the O_2 treatment. Since the thermal stability of carbonate species is not expected to be largely different in either He or O_2, the two bands are not likely due to carbonates. Second, since the rods and cubes both show similar carbonate features in the CO-TPR-IR at 773 K, then similar Raman spectra would be expected for rods and cubes if the two broad Raman bands are due to carbonate species. This is not the case as shown in Fig. 7C, which compares the Raman spectra of all three ceria nanoshapes before and after CO-TPR to 773 K. In contrast to the rods, the two bands on cubes and octahedra are extremely weak in comparison with the ceria F_{2g} mode at around 462 cm^{-1}. Therefore, both observations suggest that the bands at 1350 and 1600 cm^{-1} are not due to carbonate species. Instead, the complete burn off in O_2 makes it reasonable to assign the Raman features to the D and G modes of carbonaceous species, respectively [55,56]. The carbonaceous species are originated from the CO disproportionation or Boudouard reaction:

$$CO + CO \rightarrow CO_2 + C \tag{4}$$

which has been previously observed on reduced ceria surfaces upon interaction with CO [57–60].

Interestingly, the amount of carbonaceous species is very small on both octahedra and cubes based on the weak D and G bands. The recent detailed study of the mechanism of CO disproportionation on ceria surface [57] suggested that two CO molecules adsorbed on adjacent Ce sites and the presence of reduced Ce^{3+} sites are favorable for the CO disproportionation. The Ce^{3+} sites provide electron back-donation to weaken the C–O bond of adsorbed CO. Thus the large amount of carbonaceous species formed on ceria rods, i.e., facile CO disproportionation reaction, implies

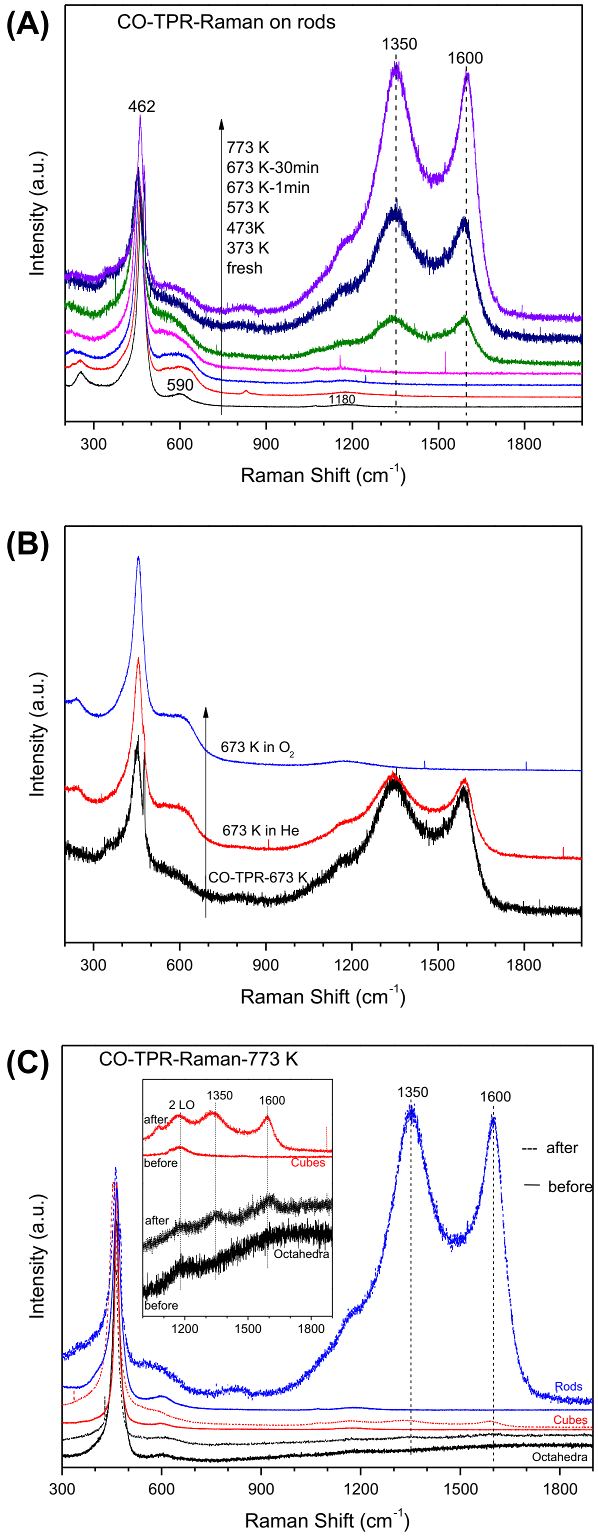

Fig. 7. (A) Raman spectra collected during CO-TPR on ceria rods. (B) Raman spectra of ceria rods after CO-TPR to 673 K and subjected to He and O_2 purging at 673 K. (C). Comparison of Raman spectra of ceria rods, cubes and octahedra after CO-TPR to 773 K. Inset shows the enlarged spectral region for carbonaceous species on cubes and octahedra. Solid spectra are collected before CO-TPR while dashed ones are collected after CO-TPR to 773 K. (For color interpretation in this figure the reader is referred to see the web version of this article.)

that there are more abundant Ce^{3+} sites on the rods surface than the cubes and octahedra surfaces, consistent with the easier reduction of ceria rods as observed in the CO-TPR profiles.

3.5. Oxygen isotopic exchange

Temperature-programmed isotopic exchange between $^{18}O_2$ and lattice ^{16}O in ceria nanoshapes was carried out in order to gain information on the mobility of lattice oxygen. Similar experiments have been reported on polycrystalline ceria, and two mechanisms were proposed for the isotopic exchange [61]. One is simple heteroexchange between $^{18}O_2$ and only one lattice oxygen anion, leading to both gaseous $^{16}O^{18}O$ and $^{16}O_2$. The second one is multiple heteroexchange where two lattice oxygen anions participate in the exchange with $^{18}O_2$, leading to only $^{16}O_2$. As shown in Fig. 8, the evolution of both $^{16}O^{18}O$ and $^{16}O_2$ was monitored during the isotopic exchange up to 1100 K. In general, the $^{16}O_2$ isotopomer is produced at lower temperature than $^{16}O^{18}O$ on all the samples, indicating that the multiple exchange mechanism is favored over simple exchange [61]. The lower the isotopomer evolution temperature is, the higher is the lattice oxygen mobility. In this respect, the oxygen isotopomers are produced at lowest temperature on rods, followed by cubes, with octahedra at much higher temperature (almost 200 K higher). For all nanoshapes, exchange of both surface and bulk oxygen is evident from the Raman spectra (see Fig. S4 for the rods as an example) where the F_{2g} and 2LO modes of bulk ceria show clear isotopic shift after the exchange reaction.

3.6. In situ IR study of CO oxidation

In situ IR spectroscopy combined with QMS was employed to follow both the CO oxidation light-off process and steady state reaction. Fig. 9A shows the IR spectra obtained as the ceria rods are heated in reactant mixture and then held at 693 K. The CO consumption and CO_2 evolution followed by online QMS are shown in Fig. 9B. IR spectra collected at temperature below 573 K are very similar to the corresponding spectra obtained during the CO-TPR (Fig. 6) process, i.e., appearance of formate species upon heating as indicated by the peaks in the C–H stretching region. Bicarbonate is also present as evidenced by the sharp peaks at 1395 and 1216 cm^{-1}. At temperature of 573 K and above, gas phase CO_2 peaks start to appear and keep increasing in intensity with temperature, consistent with the increasing production of CO_2 as followed by QMS (Fig. 9B) and thus the onset of CO oxidation on ceria rods. It is noteworthy that the broad elevated background observed in CO-TPR-IR at 673 K is absent under CO oxidation conditions (O_2:CO = 1:4) up to 693 K, implying that the ceria surface remains oxidized. After CO oxidation at 693 K for 30 min, the bicarbonate

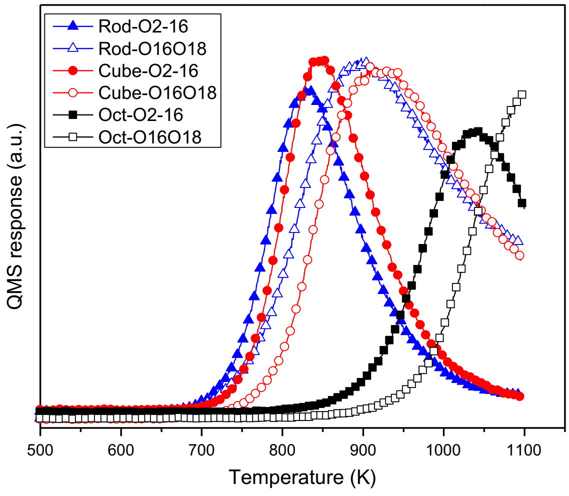

Fig. 8. QMS profiles of O_2 isotopomers, $^{16}O_2$ and $^{16}O^{18}O$, during oxygen isotopic exchange over ceria rods, cubes, and octahedra.

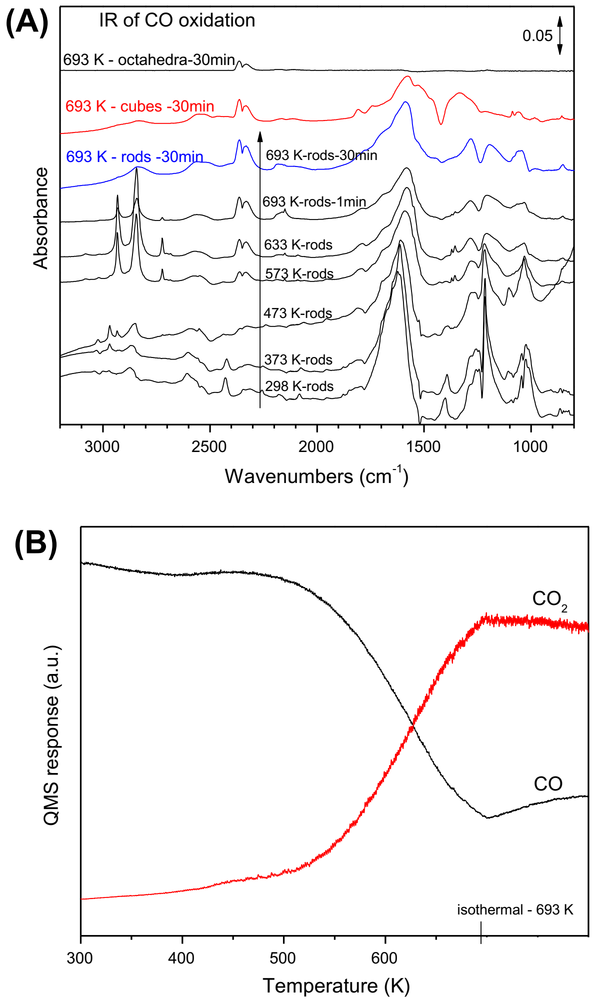

Fig. 9. (A) IR spectra collected during CO oxidation light-off on ceria rods and spectra collected at 693 K after CO oxidation for 30 min on three ceria nanoshapes. Spectra are referenced to the background spectra collected at the indicated temperature during cooling down from pretreatment process of the ceria sample. (B) Online QMS monitoring of CO oxidation light-off process on ceria rods.

and formate are absent and the spectrum is dominated by bands that can be assigned primarily to bidentate carbonate (1584, 1283, 1040, and 853 cm^{-1}), bridged carbonate (1698, 1201, and 1040 cm^{-1}), and minor unidentate carbonate (1446, 1283, 1060, and 853 cm^{-1}) in addition to the gaseous CO_2 peaks. In a separate Raman measurement of ceria rods during CO oxidation at 693 K (spectra not shown), the Raman spectrum collected under CO oxidation condition is very similar to that of freshly calcined rods. When the O_2 is switched off, leaving CO as the only reactant, Raman bands at 1350 and 1600 cm^{-1}, due to carbonaceous species, grow in. These features disappear when the O_2 is switched back in, i.e., co-feeding CO and O_2. It is clear that the surfaces of the rods are oxidized and free from carbonaceous deposits under current CO oxidation conditions.

IR spectra obtained on all three ceria nanoshapes during steady state CO oxidation at 693 K are also compared in Fig. 9A. Strong IR bands due to surface carbonate species are observed on both rods and cubes while the spectrum from octahedra shows little sign of surface carbonate. Again, this agrees well with the CO-TPD and CO-TPR results where carbonate species are strongly bound on surfaces of rods and cubes while weakly held on octahedra.

To further investigate the role of surface carbonate and carbonaceous species in CO oxidation, labeled $^{18}O_2$ was used in CO oxidation over ceria rods sample and the results from *in situ* IR and QMS are shown in Fig. 10A and B. The rods sample was pretreated at 693 K in $^{16}O_2$/He and purged with He before exposure to CO + $^{18}O_2$ at 693 K. $C^{16}O_2$ is immediately observed and dominates the product as seen by both IR and QMS at the start of the reaction. The IR spectra are essentially the same as those from CO oxidation with $^{16}O_2$, i.e., the appearance of gas phase $C^{16}O_2$ (2362 and 2332 cm^{-1}), bidentate (1585, 1275, 1210, 1040, and 852 cm^{-1}), bridged (1678, 1210, and 1040 cm^{-1}), and unidentate (1446, 1275, 1040, and 852 cm^{-1}) carbonate species. This clearly demonstrates that CO oxidation over ceria undergoes a redox mechanism, i.e., CO reacts with lattice oxygen ($^{16}O_L$) of ceria even in the presence of gaseous $^{18}O_2$. As the reaction proceeds further, the IR spectra start to show additional peaks of gaseous $C^{16}O^{18}O$ (2342 and 2322 cm^{-1}). This is consistent with the QMS observations where $C^{16}O_2$ gradually decreases in partial pressure while $C^{16}O^{18}O$ increases steadily and dominates the CO_2 isotopomers at prolonged reaction time. The production of $C^{16}O^{18}O$ is expected since the gas phase $^{18}O_2$ would gradually refill the oxygen vacancy created by initial CO oxidation and then participate in subsequent CO oxidation. Interestingly, only some of the IR bands due to surface carbonate species show isotopic shift during the reaction process but at a very slow pace. Specifically, gradual redshifts are seen within 100 min for following bands due to unidentate carbonate: 1446–1433 cm^{-1}, 1275–1268 cm^{-1}, 1040–1022 cm^{-1}, and 852–847 cm^{-1}. It appears that only this type of carbonate

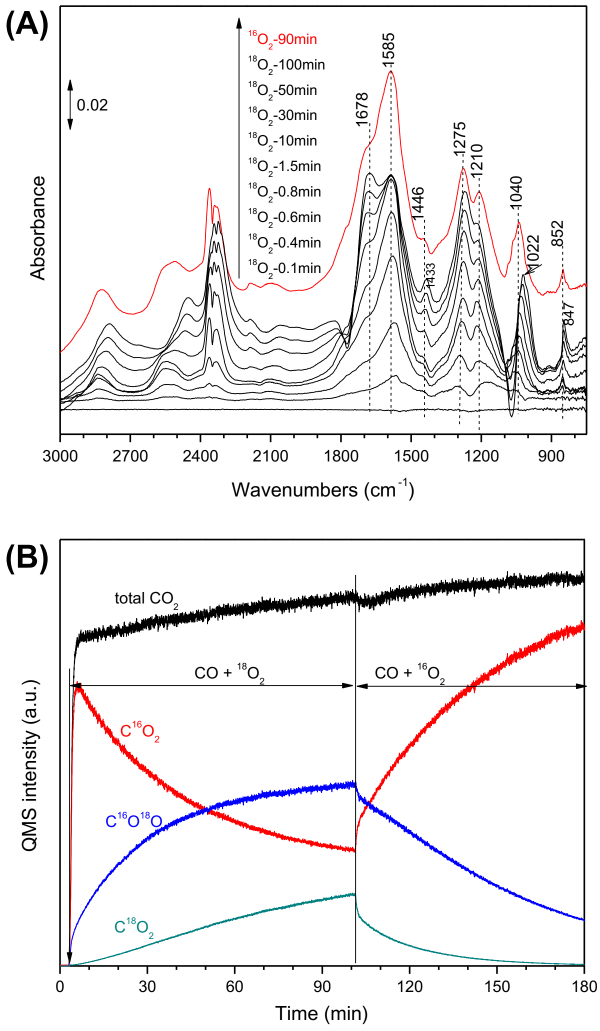

Fig. 10. IR spectra (A) and QMS profiles (B) collected during CO oxidation with $^{18}O_2$ and switching to CO oxidation with $^{16}O_2$ over ceria rods at 693 K. IR spectra are referenced to the background spectrum collected at 693 K in helium before introducing the reaction feeds.

species can undergo scrambling with isotopically labeled gas phase carbon dioxide and lattice oxygen, leading to the observed isotopic shift. The bidentate and bridged carbonate species are stable and inert to the exchange.

During CO + $^{18}O_2$ reaction, $C^{18}O_2$ is also observed to increase with reaction time in the QMS profiles, although it is the minor portion of all CO_2 isotopomers. It could also be produced *via* exchange reaction between carbon dioxide with isotopically scrambled surface carbonate species that slowly develop with time. Another possibly faster route to $C^{18}O_2$ is the direct oxidation of carbonaceous species (from transient CO disproportionation reaction) by reaction with $^{18}O_2$ or with two adjacent isotopically labeled lattice oxygen anions.

Upon switching from CO + $^{18}O_2$ to CO + $^{16}O_2$ (top curve in Fig. 10A), the redshifted IR bands shift slowly (about 90 min) back to their original frequencies as the isotopically scrambled carbonate species undergo exchange with the increasingly dominant $C^{16}O_2$ product. As expected, the $C^{16}O^{18}O$ and $C^{18}O_2$ isotopomers decrease in partial pressure after the switch (Fig. 10B).

Since CO oxidation proceeds *via* a redox mechanism, i.e., CO reduction of ceria followed by ceria reoxidation by O_2, insights into the reaction intermediate maybe gained by conducting transient gas switching between CO and O_2 during CO oxidation. The IR spectra collected during such switching on ceria rods at 693 K are shown in Fig. 11A. The carbonate species generated during CO oxidation are pretty stable under either He or O_2 purging at 693 K (compare curves *a*–*c*) as their IR bands intensity does not change much in comparison with the one under reaction condition, indicating they are not actively participating in the CO oxidation reaction cycle. Upon switching from CO oxidation to CO alone at 693 K (curve *d*), an obvious increase in background is observed from 1500 to 3000 cm^{-1}, due to reduction of ceria. There is also an increase in the total intensity in the carbonate features as well as changes in their relative intensities, indicating that CO reduction causes an increase in carbonate species and changes in their speciation. Specifically, IR features due to unidentate carbonate (1401, 1080, 865 cm^{-1}) and bridged carbonate (1782, 1401, 1190 cm^{-1}) increase in intensity in relative to those of bidentate carbonate species that dominate under CO oxidation condition. Switching from CO to He purging (curve *e*) has little effect except for a moderate decrease in the band at 1590 cm^{-1}. However, subsequent purging in O_2 brings the spectrum contour back to the one under CO oxidation, namely, the IR bands at 1782 and 1401 cm^{-1} nearly disappear while the one at 1590 cm^{-1} further declines in intensity. A downward tailing is observed in the low wavenumber region (<1100 cm^{-1}), likely due to the background change caused by the reoxidation of the reduced ceria by O_2.

The transient switch from CO to $^{16}O_2$ shown in Fig. 11A (curve *f*) leads to evolution of CO_2 as shown in the QMS profile in Fig. 11B (left side). If instead the switch is performed with isotopically labeled $^{18}O_2$, the IR spectra are essentially the same as those obtained with $^{16}O_2$ purging (Fig. 11A). But the QMS profile shows the production of isotopically labeled $C^{16}O^{18}O$ and $C^{18}O_2$ in addition to the unlabeled $C^{16}O_2$ (Fig. 11B right side). Considering the different shapes of the QMS profiles of the three CO_2 isotopomers, two sources for CO_2 production can be proposed. One is the decomposition of surface carbonate species as evident by the decreased IR bands intensity of carbonate species upon O_2 purging. These carbonate species (unidentate and bridged carbonate) must be associated with reduced ceria and would decompose to release $C^{16}O_2$ once the reduced ceria is oxidized by O_2. A similar phenomenon was observed on ceria-zirconia system by QMS and IR spectroscopy [62,63]. A second source of CO_2 is the oxidation of carbonaceous species formed from CO disproportionation reaction at 693 K as demonstrated in the CO-TPR-Raman study. The oxygen isotopic exchange results (Fig. 8) show that the lattice oxygen of rods can start to exchange isotopically with $^{18}O_2$ at 693 K. This would be promoted especially when the rods are reduced by CO. Thus the scrambled ceria lattice oxygen can oxidize the surface carbonaceous species at 693 K (as shown in the Raman results, Fig. 7B) to give the three CO_2 isotopomers. The relative amount of each CO_2 isotopomer is proportional to the population of labeled lattice oxygen around the carbonaceous species. The delayed production of $C^{18}O_2$ in comparison with $C^{16}O_2$ and $C^{16}O^{18}O$ is due to the fact that it takes longer time to formulate two labeled lattice oxygen ($^{18}O_L$) adjacent to the C atoms than just having two $^{16}O_L$ (to give $C^{16}O_2$), or one $^{16}O_L$ and one $^{18}O_L$ (to give $C^{16}O^{18}O$) around the C atoms. Apparently, $C^{16}O_2$ can be produced by both carbonates decomposition and oxidation of carbonaceous species upon O_2 purging.

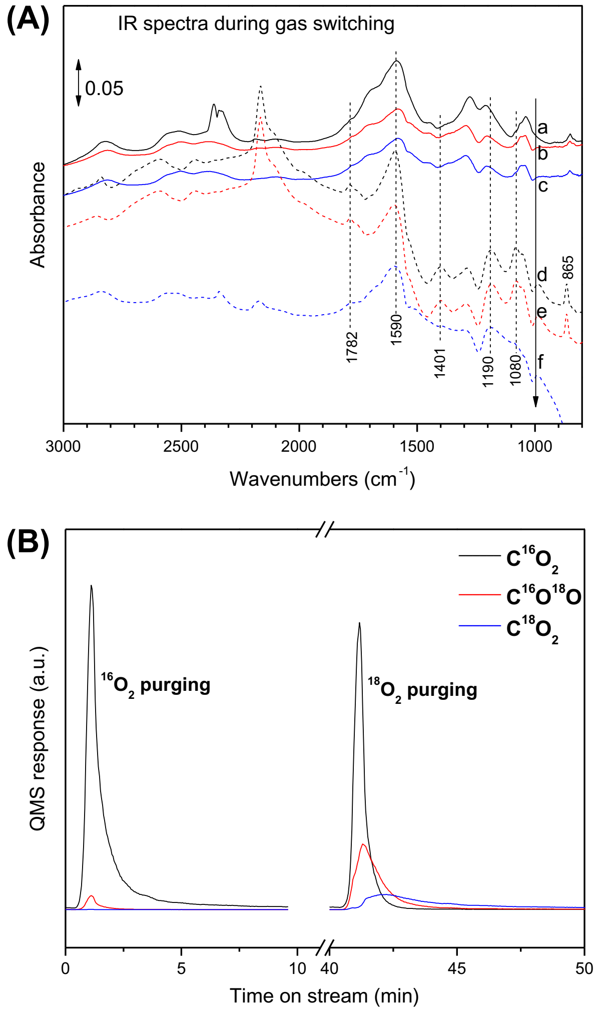

Fig. 11. (A) IR spectra collected during gas switching on ceria rods at 693 K. (a) CO oxidation, (b) He purging for 10 min after CO oxidation; (c) O_2 purging for 10 min after CO oxidation; (d) CO flow for 20 min after CO oxidation; (e) He purging for 10 min after CO flow; (f) O_2 purging after (e). IR spectra are referenced to the background spectrum collected at 693 K in helium before introducing the reaction feeds. (B) Evolution of CO_2 isotopomers during $^{16}O_2$ and $^{18}O_2$ purging at 693 K after CO flow for 20 min and He purging for 10 min over ceria rods, i.e., CO_2 evolution corresponding to spectrum (f) in 11 (A). (For color interpretation in this figure the reader is referred to see the web version of this article.)

4. Discussion

4.1. Surface structure dependence of CO oxidation

There has been renewed interest in CO oxidation over ceria because the recent successful synthesis of ceria nanocrystals with different morphologies offers opportunities to study the surface structure dependence of CO oxidation over ceria catalysts. It was shown that ceria rods [15,20,28,30,64], nanowires [28,64], and nanotubes [64,65] exposing {1 1 0} and/or {1 0 0} surfaces outperform their counterpart irregular nanoparticles in CO oxidation in terms of light-off temperature. The oxygen storage capacity was reported to follow the order of cubes > rods ≫ polyhedra but their corresponding CO oxidation activity was not systematically compared [16,66]. Our results here present a direct comparison of CO oxidation performance of the three common ceria surfaces, {1 1 0}, {1 0 0}, and {1 1 1} by utilizing ceria nanoshapes with well-defined surface planes. The light-off temperature is the lowest on rods, closely followed by cubes, and the highest on octahedra. Furthermore, the TOF of CO oxidation also follows the order of {1 1 0} > {1 0 0} ≫ {1 1 1}. This gives clear evidence that CO oxidation is strongly surface structure dependent over ceria catalysts. The result is well supported by both previous theoretical work and our detailed spectroscopic studies. The oxygen vacancy formation energy was predicted to follow the reverse order of lattice oxygen reactivity: {1 1 0} < {1 0 0} < {1 1 1} [33,34] since the less energy that is needed to form an oxygen vacancy, the more reactive is the surface plane toward a CO molecule. Experimentally, the *in situ* spectroscopic investigations here provide in-depth molecular-level information about the surface dependence of CO oxidation over ceria, which is largely lacking in current literature. Specifically, we find that the interaction of CO with ceria (adsorption and reduction) and the reactivity and mobility of ceria surface and bulk oxygen are closely related to the exposed surface structure of ceria nanocrystals.

4.1.1. CO adsorption

IR spectra of CO adsorbed on the three ceria nanoshapes (Fig. 3) show the presence of two types of CO species: adsorbed CO on surface *cus* Ce^{4+} sites and CO chemically bonded to surface oxygen forming carbonate species. For the former species, CO is weakly adsorbed on the cationic Ce sites of all three surfaces and readily desorbs at rt. The larger IR band intensity on rods and cubes than on octahedra is likely the consequence of difference in both surface area (octahedra have the smallest surface area) and surface structure (Ce is more *cus* on {1 1 0} and {1 0 0} surfaces (6-coordinated) than on {1 1 1} (7-coordinated) [67]). As for carbonate species, IR results show that both the type and the thermal stability of the surface carbonates are surface dependent on the three nanoshapes. Previous DFT work [23] suggested that the formation of carbonate species upon CO adsorption on ceria surface is determined by three factors: oxygen vacancy formation energy, surface lattice oxygen coordination number and distance. It was predicted that carbonate species can only form on {1 1 0} and {1 0 0} surfaces rather than on {1 1 1} because neither of three factors is favored on the {1 1 1} surface. The DFT results support our IR results on rods and cubes that similar types of carbonate species, i.e., bicarbonate, bridged, and bidentate carbonate species are produced on the two surfaces upon CO adsorption at rt. The generation of small amount of carbonate species (bidentate and unidentate) on the octahedra, not predicted by the computational work [23,27,37] nor found in UHV experiments on $CeO_2(1 1 1)$ films [68], is possibly due to the presence of *cus* sites on edges, corners, and some defect sites inherently formed during synthesis of the octahedra nanocrystals. As a matter of fact, our recent Raman work [10] showed that some intrinsic defect sites are already present on the three types of ceria nanocrystals and their amount follows rods > cubes > octahedra. Furthermore, the microscopic graphs indicated the presence of high concentration of *cus* sites on ceria rods. The presence of *cus* and defect sites would provide the surface oxygen more flexibility in interacting with CO. So the relatively large amount of *cus* and defect sites present in rods would favor strong interaction with CO, leading to the formation of variety of surface carbonates. CO-TPD shows that the carbonate species have different thermal stability, following the sequence of rods > cubes ≫ octahedra. The thermal stability is a good indicator for how strongly CO interacts with the surface lattice oxygen on the three different surfaces. Apparently, the lowest oxygen vacancy formation energy (+1.99 eV) [33], the low coordination number (3-coordinated) of surface oxygen, the shortest surface oxygen–oxygen distance (2.74 Å) [23] on {1 1 0} surface, and the presence of largest amount of *cus* and defect sites on ceria rods [10] all favor the strongest CO adsorption and reaction with the surface oxygen on ceria. Although similar types of carbonate species, e.g., bidentate carbonate species, are formed on the three nanoshapes, their thermal stability is not the same. So the thermal stability of the carbonate species is not only determined by their types but also directly related to the surface structure of ceria where they are bonded to.

It is necessary to point out that a carbonate-free ceria surface requires pretreatment temperatures above 1000 K [1]. The surface of all the ceria nanoshapes calcined at 673 K in our study may still be partially occupied by certain stable carbonate species. Thus rt CO adsorption is actually probing what has been left unoccupied on the ceria surface. Although this makes it difficult to provide a complete picture of the individual surface planes of ceria nanoshapes, IR investigation of CO adsorption and desorption is still meaningful for understanding CO oxidation because the reaction also takes place on the same surfaces that may be partially occupied with stable carbonate species.

4.1.2. CO-TPR

The low-temperature reduction regime (<850 K) in the CO-TPR profiles of ceria nanoshapes is generally due to the surface oxygen removal by CO and thus is closely relevant to CO oxidation reaction. The reduction temperature from both CO-TPR and CO-TPR-IR (elevated IR background characterizing the reduction of ceria) shows surface dependence with rods < cubes < octahedra, in general agreement with the onset of CO oxidation activity (Fig. 2). This implies that the reduction of surface lattice oxygen is the rate determining step in CO oxidation on ceria catalysts. The *in situ* IR and Raman spectroscopic results provide information on the surface chemistry that occurs during the low-temperature (<850 K) CO-TPR process. The CO_2 evolution in CO-TPR low-temperature regime is determined to be derived from four reaction channels: direct CO reduction of surface lattice oxygen (channel A), desorption of carbonate species formed during low-temperature CO adsorption (channel B), surface water–gas shift reaction between CO and hydroxyl groups (channel C), and CO disproportionation reaction (channel D). The former three channels all involve CO reduction of ceria surface while the last channel, CO disproportionation, does not. It is interesting to define the contribution of each channel to CO_2 production and determine how it varies on the three different ceria nanoshapes.

Since the surface water–gas shift reaction generates over 50% of the total low-temperature CO_2 (Table S1) in the TPR process, this route (channel C) is the predominate channel in producing CO_2 on all three ceria nanoshapes. Although this reaction has been reported on ceria surfaces [49,50], its contribution has rarely been quantified to the low-temperature regime CO_2 production in CO-TPR. The *in situ* CO-TPR-IR spectra shown in Fig. 6 support the occurrence of such surface reaction because formate and formyl species, likely products from the reaction between surface hydroxyl groups and CO, are clearly observed at low temperatures and decompose at higher temperatures on the surface of three ceria nanoshapes. Concurrently, the IR spectra background gradually elevates, signaling the reduction of ceria surface.

The contribution from carbonates decomposition (channel B) to CO_2 evolution is rather limited and shows up at temperature below 700 K. This is mostly evident when the CO-TPD (Fig. 4) and CO-TPR

(Fig. 5A) profiles are overlaid and compared (see Fig. S5). Since these decomposed carbonate species are originated from rt CO adsorption, they represent the most reactive surface oxygen to CO. It appears from Fig. S5 that the amount of these reactive surface lattice oxygen follows the trend rods > cubes > octahedra.

Channel A, direct CO reaction with surface lattice oxygen, contributes to CO_2 production in the intermediate temperature range from 400 to 700 K in CO-TPR process since channels C and D proceed at relatively higher temperatures ($\geqslant$673 K) while channel B contributes most to the lower temperature range. The reactivity of this type of surface oxygen, other than the most active surface lattice oxygen in channel B and surface hydroxyls in channel C, appears similar on both rods and cubes, but is less on octahedra because both cubes and rods show an intermediate temperature CO_2 evolution peak ($\sim$570 K) while octahedra does not.

The contribution from CO disproportionation (channel D) for CO_2 production is mainly at higher temperature range ($\geqslant$673 K) according to the CO-TPR-Raman study (Fig. 7). Its contribution is difficult to quantify, even if isotopically labeled $C^{18}O$ or $Ce^{18}O_2$ is used, due to the active scrambling among oxygen isotopomers at such high temperature on ceria surface [60]. But, it is believed to be insignificant on the cubes and octahedra surfaces, and was even not observed in previous literature reports on polycrystalline ceria [50]. Its contribution is clearly the largest on ceria rods as inferred from the amount of surface carbonaceous species detected by *in situ* CO-TPR-Raman. It is interesting that the CO disproportionation reaction happens to much larger degree on ceria rods than on cubes, since these two nanoshapes show similar CO adsorption and desorption behavior. Recalling that CO disproportionation reaction requires two adjacent Ce sites and is facilitated by reduced ceria surface [57–60], we conclude that since the rods and cubes surfaces are both reduced to some extent up to 773 K, the difference is likely related to the different nature of the defect sites induced by the reduction on the two nanoshapes. Our recent Raman results demonstrated that the defect sites (oxygen vacancies) are more clustered on rods surface than on cubes after 673 K reduction [10], and this clustering on the rods therefore explains their greater ability for CO disproportionation and carbonaceous species buildup. The clustering of defect sites was also found beneficial for CO oxidation in a recent study of two types of ceria nanorods with different defect sites density [11] and may thus be accountable for the better CO oxidation activity on our ceria rods.

4.1.3. Lattice oxygen mobility

The reactivity of surface lattice oxygen has been well revealed by the CO-TPR study as discussed above. Since the reactivity of lattice oxygen and oxygen storage capability were found to be enhanced by high oxygen mobility [42,61], the mobility of lattice oxygen plays an important role in ceria catalysis. This property of the three ceria nanoshapes is accessed by the oxygen isotopic exchange study (Fig. 8), which shows that the oxygen mobility follows the sequence of rods > cubes $\gg$ octahedra. The underlying reason for the high mobility of lattice oxygen on rods and cubes is that the amount of intrinsic defect sites in the two nanoshapes is much higher than in octahedra [10]. The presence of defect sites, i.e., oxygen vacancies, provides relative freedom for the movement of lattice oxygen and thus increases the mobility of oxygen in ceria. Because the amount of defect sites is determined by the surface planes of ceria nanoshapes [10], the oxygen mobility is thus surface dependent on ceria and promotes oxygen reactivity to CO as observed in the CO oxidation reaction.

4.2. Mechanism of CO oxidation

It has been well accepted that CO oxidation proceeds on ceria catalysts *via* redox (Mars–van Krevelen) mechanism [1]. Our *in situ* IR-QMS (Fig. 10) result using isotopically labeled $^{18}O_2$ in CO oxidation on ceria rods agrees well with this mechanism, i.e., initial dominance of $C^{16}O_2$ generated *via* CO reaction with the ceria lattice oxygen ($^{16}O_L$) and then slow evolution of isotopically labeled CO_2 due to the refilling of oxygen vacancies by the gas phase $^{18}O_2$. Furthermore, our *in situ* spectroscopic results shed light on the reaction pathway and reaction intermediates of CO oxidation over ceria catalysts.

Although the CO-TPR process can have four different channels for the formation of CO_2, there could be only two pathways for high-temperature CO oxidation: CO reaction with lattice oxygen and CO disproportionation. Surface water–gas shift reaction would not be sustainable as the surface hydroxyl groups are no longer available once consumed. The reaction between CO and lattice oxygen is evident from the IR-QMS study of CO + $^{18}O_2$ over ceria rods (Fig. 10) and is generally considered the major pathway for CO oxidation over ceria catalysts. Three channels can happen in this main reaction pathway. The first is direct CO reaction with lattice oxygen to form gaseous CO_2 (see reaction (3)), as observed in the steady state reaction and transient switch from CO oxidation to CO. Due to the fast rate of this channel, no reaction intermediate information is obtainable in the spectroscopic studies. The second channel is decomposition of carbonate species associated with reduced ceria. In this channel, CO_2 is released upon reoxidation of the reduced ceria by O_2 and is evident in the transient switching between CO, He and O_2 (Fig. 11). These carbonate species (likely bridged and unidentate carbonate) associated with reduced ceria are not stable under CO oxidation condition and not observable by our IR spectroscopy, but they could be considered among the reaction intermediates in CO oxidation to CO_2. In previous studies of ceria and ceria-zirconia catalysts [62,69] under cycled feed-stream condition of CO and O_2, these two channels for CO_2 production were also proposed. In the third channel, a portion of the carbonate species formed on oxidized ceria surface decomposes under CO oxidation condition. Since only a fraction of the carbonates (unidentate carbonate species) undergoes isotopic exchange at a very slow pace (Fig. 10), this fraction may play a very limited role in CO oxidation and must be regarded as minor intermediate in CO oxidation. The majority of the carbonate observed under CO oxidation conditions does not participate in the isotopic exchange and seems to represent a stable spectator in CO oxidation. This also explains why the ceria rods and cubes are still showing high activity in CO oxidation despite the strongly held carbonate species on their surfaces.

The occurrence of CO disproportionation reaction under CO oxidation condition is difficult to determine. The absence of surface carbonaceous species under steady state reaction condition (from Raman) cannot exclude that CO disproportionates since the generated carbon can be readily oxidized to CO_2 at the reaction temperature. Due to the fast isotopic exchange between CO and ceria [60] at CO oxidation temperature, the use of isotopically labeled CO or ceria would not help to confirm whether CO disproportionation occurs or not. Considering the fact that the ceria surface is kept oxidized under our CO oxidation condition while CO disproportionation is facilitated by reduced ceria surface [57–60], the contribution from CO disproportionation to CO_2 formation may be limited under CO oxidation condition and would follow the trend rods > cubes, octahedra.

5. Conclusions

The surface structure dependence of CO oxidation over three ceria nanoshapes, rods, cubes, and octahedra, was clearly shown and further investigated in detail by using *in situ* IR and Raman spectroscopy coupled with online QMS, CO-TPR, oxygen isotopic exchange and isotopic labeling techniques. Following conclusions can be drawn from these investigations:

(1) Different types of carbonate species are formed from adsorption of CO at rt on the ceria nanoshapes. The carbonate species are similar in nature on the more reactive rods and cubes surfaces ({110} and {100}) and are more strongly bonded than on the less reactive octahedra surface ({111}).
(2) *In situ* spectroscopy results show that several reaction routes occur during CO-TPR of ceria nanoshapes, i.e., CO removal of lattice oxygen, surface water–gas shift reaction, and CO disproportionation. The contribution of these routes to CO_2 production is dependent on the surface planes of ceria.
(3) The lattice oxygen reactivity (accessed by CO-TPR) and mobility (accessed by oxygen isotopic exchange) are strongly surface dependent, following the same trend as in CO oxidation: rods > cubes ≫ octahedra.
(4) The differences in surface oxygen vacancy formation energy, nature and amount of low coordination sites and defect sites, ultimately affected by the surface planes of ceria nanoshapes, are believed to be the driving forces for the surface-dependent behaviors of CO interaction with ceria, lattice oxygen reactivity and mobility, and thus the CO oxidation performance.
(5) The reaction pathways and reaction intermediates of CO oxidation over ceria nanoshapes are revealed by the *in situ* IR and Raman investigations. CO_2 is generated *via* direct CO reaction with lattice oxygen, decomposition of carbonate species, and possibly CO disproportionation. Certain surface carbonate species, mainly those associated with reduced ceria surface, are possibly among the reaction intermediates. Majority of the carbonate species observed under steady state CO oxidation condition are reaction spectators.

Acknowledgments

This Research is sponsored by the Division of Chemical Sciences, Geosciences, and Biosciences, Office of Basic Energy Sciences, US Department of Energy. Part of the work including Raman and TEM/SEM was conducted at the Center for Nanophase Materials Sciences, which is sponsored at Oak Ridge National Laboratory, by the Office of Basic Energy Science, US Department of Energy. The research was supported in part by the appointment for M.J. Li to the ORNL Postdoctoral Research Associates Program, administered jointly by ORNL and the Oak Ridge Associated Universities.

Appendix A. Supplementary material

Supplementary data associated with this article can be found, in the online version, at doi:10.1016/j.jcat.2011.09.011.

References

[1] A. Trovarelli, Catal. Rev. – Sci. Eng. 38 (1996) 439–520.
[2] C. Binet, M. Daturi, J.C. Lavalley, Catal. Today 50 (1999) 207–225.
[3] L. Vivier, D. Duprez, Chemsuschem 3 (2010) 654–678.
[4] J. Beckers, G. Rothenberg, Green Chem. 12 (2010) 939–948.
[5] C. Ratnasamy, J.P. Wagner, Catal. Rev. – Sci. Eng. 51 (2009) 325–440.
[6] D. Duprez, C. Descorme, T. Birchem, E. Rohart, Top. Catal. 16 (2001) 49–56.
[7] J.A. Rodriguez, S. Ma, P. Liu, J. Hrbek, J. Evans, M. Perez, Science 318 (2007) 1757–1760.
[8] J. Guzman, S. Carrettin, A. Corma, J. Am. Chem. Soc. 127 (2005) 3286–3287.
[9] R. Si, M. Flytzani-Stephanopoulos, Angew. Chem. – Int. Ed. 47 (2008) 2884–2887.
[10] Z.L. Wu, M.J. Li, J. Howe, H.M. Meyer, S.H. Overbury, Langmuir 26 (2010) 16595–16606.
[11] X.W. Liu, K.B. Zhou, L. Wang, B.Y. Wang, Y.D. Li, J. Am. Chem. Soc. 131 (2009) 3140–3141.
[12] B. Murugan, A.V. Ramaswamy, J. Am. Chem. Soc. 129 (2007) 3062–3063.
[13] P. Dutta, S. Pal, M.S. Seehra, Y. Shi, E.M. Eyring, R.D. Ernst, Chem. Mater. 18 (2006) 5144–5146.
[14] F. Esch, S. Fabris, L. Zhou, T. Montini, C. Africh, P. Fornasiero, G. Comelli, R. Rosei, Science 309 (2005) 752–755.
[15] K.B. Zhou, X. Wang, X.M. Sun, Q. Peng, Y.D. Li, J. Catal. 229 (2005) 206–212.
[16] H.X. Mai, L.D. Sun, Y.W. Zhang, R. Si, W. Feng, H.P. Zhang, H.C. Liu, C.H. Yan, J. Phys. Chem. B 109 (2005) 24380–24385.
[17] E. Aneggi, J. Llorca, M. Boaro, A. Trovarelli, J. Catal. 234 (2005) 88–95.
[18] H. Imagawa, A. Suda, K. Yamamura, S. Sun, J. Phys. Chem. C 115 (2011) 1740–1745.
[19] G.S. Zafiris, R.J. Gorte, J. Catal. 143 (1993) 86–91.
[20] H.P. Zhou, Y.W. Zhang, R. Si, L.S. Zhang, W.G. Song, C.H. Yan, J. Phys. Chem. C 112 (2008) 20366–20374.
[21] M.N. Guo, C.X. Guo, L.Y. Jin, Y.J. Wang, J.Q. Lu, M.F. Luo, Mater. Lett. 64 (2010) 1638–1640.
[22] B.T. Teng, S.Y. Jiang, X.W. Guo, J.H. Yuan, M.F. Luo, Acta Chim. Sinica 67 (2009) 2765–2772.
[23] M. Nolan, G.W. Watson, J. Phys. Chem. B 110 (2006) 16600–16606.
[24] M. Nolan, V.S. Verdugo, H. Metiu, Surf. Sci. 602 (2008) 2734–2742.
[25] M. Nolan, J. Phys. Chem. C 113 (2009) 2425–2432.
[26] C. Muller, B. Paulus, K. Hermansson, Surf. Sci. 603 (2009) 2619–2623.
[27] M. Huang, S. Fabris, J. Phys. Chem. C 112 (2008) 8643–8648.
[28] Tana, M.L. Zhang, J. Li, H.J. Li, Y. Li, W.J. Shen, Catal. Today 148 (2009) 179–183.
[29] L. Yan, R.B. Yu, J. Chen, X.R. Xing, Cryst. Growth Des. 8 (2008) 1474–1477.
[30] Y.J. Guan, E.J.M. Hensen, Y. Liu, H.D. Zhang, Z.C. Feng, C. Li, Catal. Lett. 137 (2010) 28–34.
[31] K.S. Lin, S. Chowdhury, Int. J. Mol. Sci. 11 (2010) 3226–3251.
[32] W.Q. Han, W. Wen, J.C. Hanson, X.W. Teng, N. Marinkovic, J.A. Rodriguez, J. Phys. Chem. C 113 (2009) 21949–21955.
[33] M. Nolan, J.E. Fearon, G.W. Watson, Solid State Ionics 177 (2006) 3069–3074.
[34] M. Nolan, S.C. Parker, G.W. Watson, Surf. Sci. 595 (2005) 223–232.
[35] D.O. Scanlon, N.M. Galea, B.J. Morgan, G.W. Watson, J. Phys. Chem. C 113 (2009) 11095–11103.
[36] M.K. Alam, F. Ahmed, K. Nakamura, A. Suzuki, R. Sahnoun, H. Tsuboi, M. Koyama, N. Hatakeyama, A. Endou, H. Takaba, C.A. Del Carpio, M. Kubo, A. Miyamoto, J. Phys. Chem. C 113 (2009) 7723–7727.
[37] Z.X. Yang, T.K. Woo, K. Hermansson, Chem. Phys. Lett. 396 (2004) 384–392.
[38] M.L. Granados, F.C. Galisteo, P.S. Lambrou, R. Manscal, J. Sanz, I. Sobrados, J.L.G. Fierro, A.M. Efstathiou, J. Catal. 239 (2006) 410–421.
[39] Z.L. Wu, S.H. Zhou, H.G. Zhu, S. Dai, S.H. Overbury, J. Phys. Chem. C 113 (2009) 3726–3734.
[40] Z.L. Wu, S.H. Zhou, H.G. Zhu, S. Dai, S.H. Overbury, Chem. Commun. (2008) 3308–3310.
[41] Z.L. Wu, S. Dai, S.H. Overbury, J. Phys. Chem. C 114 (2010) 412–422.
[42] Y. Madier, C. Descorme, A.M. Le Govic, D. Duprez, J. Phys. Chem. B 103 (1999) 10999–11006.
[43] C. Li, Y. Sakata, T. Arai, K. Domen, K. Maruya, T. Onishi, J. Chem. Soc. – Faraday Trans. I 85 (1989) 929–943.
[44] O. Pozdnyakova, D. Teschner, A. Wootsch, J. Krohnert, B. Steinhauer, H. Sauer, L. Toth, F.C. Jentoft, A. Knop-Gericke, Z. Paal, R. Schlogl, J. Catal. 237 (2006) 1–16.
[45] C. Li, Y. Sakata, T. Arai, K. Domen, K.I. Maruya, T. Onishi, J. Chem. Soc. – Faraday Trans. I 85 (1989) 1451–1461.
[46] P. Bera, A.L. Camara, A. Hornes, A. Martinez-Arias, J. Phys. Chem. C 113 (2009) 10689–10695.
[47] G. Busca, V. Lorenzelli, Mater. Chem. 7 (1982) 89–126.
[48] T. Shido, Y. Iwasawa, J. Catal. 136 (1992) 493–503.
[49] F.C. Meunier, D. Reid, A. Goguet, S. Shekhtman, C. Hardacre, R. Burch, W. Deng, M. Flytzani-Stephanopoulos, J. Catal. 247 (2007) 277–287.
[50] H.Q. Zhu, Z.F. Qin, W.J. Shan, W.J. Shen, J.G. Wang, J. Catal. 225 (2004) 267–277.
[51] J. Saussey, J.C. Lavalley, J. Lamotte, T. Rais, J. Chem. Soc. – Chem. Commun. (1982) 278–279.
[52] F. Boccuzzi, G. Ghiotti, A. Chiorino, J. Chem. Soc. – Faraday Trans. Ii 79 (1983) 1779–1789.
[53] A. Yamakata, T. Ishibashi, H. Onishi, Chem. Phys. Lett. 333 (2001) 271–277.
[54] W.H. Weber, K.C. Hass, J.R. Mcbride, Phys. Rev. B 48 (1993) 178–185.
[55] Z.L. Wu, P.C. Stair, J. Catal. 237 (2006) 220–229.
[56] S. Kuba, H. Knozinger, J. Raman Spectrosc. 33 (2002) 325–332.
[57] Y. Liu, C. Wen, Y. Guo, X.H. Liu, J.W. Ren, G.Z. Lu, Y.Q. Wang, Chemcatchem 2 (2010) 336–341.
[58] M. Swanson, V.V. Pushkarev, V.I. Kovalchuk, J.L. d'Itri, Catal. Lett. 116 (2007) 41–45.
[59] C. Li, Y. Sakata, T. Arai, K. Domen, K. Maruya, T. Onishi, J. Chem. Soc. – Chem. Commun. (1991) 410–411.
[60] A. Holmgren, B. Andersson, D. Duprez, Appl. Catal. B – Environ. 22 (1999) 215–230.
[61] D. Martin, D. Duprez, J. Phys. Chem. 100 (1996) 9429–9438.
[62] M. Boaro, F. Giordano, S. Recchia, V. Dal Santo, M. Giona, A. Trovarelli, Appl. Catal. B – Environ. 52 (2004) 225–237.
[63] C. Mondelli, V. Dal Santo, A. Trovarelli, M. Boaro, A. Fusi, R. Psaro, S. Recchia, Catal. Today 113 (2006) 81–86.
[64] C.S. Pan, D.S. Zhang, L.Y. Shi, J.H. Fang, Eur. J. Inorg. Chem. (2008) 2429–2436.

[65] L. Gonzalez-Rovira, J.M. Sanchez-Amaya, M. Lopez-Haro, E. del Rio, A.B. Hungria, P. Midgley, J.J. Calvino, S. Bernal, F.J. Botana, Nano Lett. 9 (2009) 1395–1400.
[66] J. Zhang, H. Kumagai, K. Yamamura, S. Ohara, S. Takami, A. Morikawa, H. Shinjoh, K. Kaneko, T. Adschiri, A. Suda, Nano Lett. 11 (2011) 361–364.
[67] M.V. Ganduglia-Pirovano, A. Hofmann, J. Sauer, Surf. Sci. Rep. 62 (2007) 219–270.
[68] D.R. Mullins, K.Z. Zhang, Surf. Sci. 513 (2002) 163–173.
[69] E. Aneggi, M. Boaro, C. de Leitenburg, G. Dolcetti, A. Trovarelli, J. Alloy. Compd. 408 (2006) 1096–1102.